Eng. Sci., 2025, **38**, 1843

Engineered Science
DOI: https://dx.doi.org/10.30919/es1843

Performance Optimisation of $CH_3NH_3SnI_3$ Based Perovskite Solar Cells: A Drift-Diffusion Approach

Zhansaya Omarova,[1,*] Yerik Merkibayev,[2,*] Bauyrzhan Bazarbay,[3] Ramina Shumakova[3] and Erik Shalenov[4]

Abstract

This study investigates the drift-diffusion behavior in tin-based perovskite solar cells, specifically focusing on $CH_3NH_3SnI_3$, with the aim of understanding how ion mobility, hysteresis, recombination mechanisms, and material parameters influence device performance. Tin-based perovskites represent a promising alternative to lead-based compounds due to their reduced toxicity and comparable optoelectronic properties, yet they pose challenges related to stability and efficiency. A numerical model was developed by solving the coupled Poisson and continuity equations, incorporating both electronic and ionic transport phenomena. The simulation framework allows for variation in ion mobility, defect density, recombination rates, and built-in potential, enabling a comprehensive analysis of dynamic and steady-state responses. The results reveal a significant dependence of hysteresis behavior on ion migration and recombination at interfaces, as well as a notable impact of ionic mobility on current–voltage characteristics and power conversion efficiency. Furthermore, the model shows that optimization of material parameters can mitigate hysteresis and enhance device stability and output. These findings provide valuable insights into the physical mechanisms limiting the performance of tin-based perovskite solar cells and suggest strategies for their improvement through targeted material and device engineering.

Keywords: Perovskite solar cells; $CH_3NH_3SnI_3$; Hysteresis index; Recombination; Drift–diffusion model.
Received: 08 October 2025; Revised: 21 October 2025; Accepted: 25 October 2025
Article type: Research article.

1. Introduction

The demand for renewable energy sources is increasing each year, leading to an acceleration of research in the field of next-generation photovoltaic technologies.[1–3] Among these, perovskite solar cells (PSCs) have emerged as a promising candidate, having rapidly achieved high power conversion efficiencies exceeding 27%.[4] This remarkable progress is primarily attributed to their exceptional optoelectronic properties, including strong optical absorption, low exciton binding energy, long carrier diffusion lengths, and tunable bandgaps.[5–10]

The recent growth of renewable energy and functional materials has led to active research in perovskite solar cells, hydrogen storage systems, and thermoelectric materials. Density functional theory (DFT) methods help predict the structural, electronic, and optical properties of promising compounds.[11–20] In particular, studies on modifying transport layers, defect passivation, and using nanostructured SnO_2 layers show significant improvements in the efficiency and stability of perovskite solar cells.[13,21–29] Amid these advances, lead-free perovskites like $CH_3NH_3SnI_3$ are gaining interest because of their good optoelectronic properties and environmental safety.[30–33] This makes them very promising for creating efficient and stable solar cells.

Among various perovskite materials, methylammonium tin iodide ($CH_3NH_3SnI_3$) has emerged as a promising candidate for the development of lead-free, environmentally friendly PSCs.[34,35] $CH_3NH_3SnI_3$ exhibits a suitable direct bandgap (~1.3 eV), high hole mobility, and favorable charge transport characteristics, making it theoretically well-suited for efficient solar energy harvesting.[36–38] However, the practical realization of high-performance $CH_3NH_3SnI_3$-based PSCs remains hindered by several material- and device-level challenges. The most critical issues include the rapid oxidation of Sn^{2+} to Sn^{4+} under ambient conditions, which leads to self-doping and carrier imbalance; a high density of intrinsic defects; and suboptimal energy level alignment at interfaces. These factors limit the open-circuit voltage (V_{OC}), reduce carrier lifetimes, and contribute to parasitic recombination losses, thereby impeding the overall efficiency and stability of the device.[39–41]

[1]*Department of Standardization, Certification and Metrology, Satbayev University, Almaty, 050013, Kazakhstan*
[2]*Department of Metallurgy and Mineral Processing, Satbayev University, Almaty, 05013, Kazakhstan*
[3]*Department of Mechanical Engineering, Satbayev University, Almaty, 05013, Kazakhstan*

One of the challenges is the pronounced hysteresis often observed in the current–voltage (J–V) characteristics of perovskite solar cells.[42–49] Hysteresis refers to the discrepancy in the J–V response depending on the scan direction (forward or reverse) and is widely recognized as a manifestation of fundamental dynamic processes, such as ion migration, charge accumulation at interfaces, and trap-assisted recombination. In $CH_3NH_3SnI_3$-based perovskite solar cells (PSCs), which exhibit heightened sensitivity to ionic mobility and defect states, the presence of hysteresis complicates the accurate determination of steady-state performance metrics and indicates instability in charge transport and recombination processes.[50–52] Therefore, a detailed understanding of the origins and effects of hysteresis is crucial not only for the reliable assessment of device performance but also for the targeted improvement of stability and reproducibility at both the material level and in the design of solar cell architectures.

To address these challenges and fully harness the potential of $CH_3NH_3SnI_3$, a deeper understanding of charge transport dynamics and loss mechanisms is essential. Numerical modeling based on the drift-diffusion framework serves as a powerful tool for analyzing and optimizing PSC performance, enabling systematic investigation of material properties and device parameters.

Modeling enables the deconvolution of internal device processes that are experimentally challenging to access and allows for the systematic variation of parameters to guide optimization strategies. In this study, a one-dimensional Driftfusion model, originally developed by Calado *et al.*,[53] is employed and extended to investigate the performance of $CH_3NH_3SnI_3$-based perovskite solar cells (PSCs). Driftfusion is a versatile and open-source simulation platform specifically designed to model the optoelectronic behavior of perovskite devices using the drift-diffusion formalism. The model incorporates charge carrier transport equations, the Poisson equation for electrostatics, and accounts for trap-assisted recombination, ion migration, and complex interfacial dynamics. This study builds upon the original Driftfusion framework by incorporating material-specific parameters relevant to tin-based perovskites, including reduced dielectric permittivity, higher intrinsic defect densities, and non-radiative recombination pathways unique to Sn-based systems. Furthermore, improvements are introduced to the model to better capture the actual behavior of $CH_3NH_3SnI_3$ devices, including:

1) Modeling dynamic ion migration, particularly accounting for the role of mobile species induced by iodide and tin vacancies;

2) Band edge shifts at the interfaces with transport layers and their impact on the built-in potential and charge extraction;

3) Non-uniform defect profiles across the absorber thickness to simulate the effects of graded doping and self-passivation;

4) Modification of surface recombination rates to investigate interface engineering strategies.

The primary objective of this study is to analyze the impact of ion-mediated recombination and ionic mobility on the hysteresis effect in $CH_3NH_3SnI_3$-based perovskite solar cells. By simulating current–voltage (J–V) characteristics under various conditions — including the presence and absence of ion-mediated recombination, as well as varying ionic mobility values — the influence of mobile ionic species on the magnitude of hysteresis and overall photovoltaic performance of the device is analyzed. To quantitatively assess the degree of hysteresis, a hysteresis index (HI) is calculated based on forward and reverse J–V scans.

To quantify the extent of hysteresis, we calculate the hysteresis index (HI) for each J–V curve based on the power conversion efficiencies (PCEs) obtained during forward and reverse voltage sweeps, following the methodology outlined in Ref. Eq. (1):[54]

$$Hysteresis\ Index\ (HI) = \frac{PCE(reverse) - PCE(forward)}{PCE(reverse)}. \quad (1)$$

Using the enhanced drift-diffusion model, a comprehensive parametric study is conducted to identify the key factors governing the operational characteristics of the device. Parameters such as absorber layer thickness, doping level, charge carrier mobility, trap state density, and interfacial recombination are systematically varied to quantitatively analyze their effects on open-circuit voltage (V_{OC}), short-circuit current density (J_{SC}), fill factor (FF), and overall power conversion efficiency (PCE).

The results obtained from the drift-diffusion process simulations not only enable the identification of key loss mechanisms and the physical origin of hysteresis but also facilitate the development of practical guidelines for the design of $CH_3NH_3SnI_3$-based perovskite solar cells. Consequently, this work contributes to the advancement of stable, highly efficient, and environmentally friendly photovoltaic technologies based on lead-free perovskites through the modeling and engineering of functional materials and heterostructures.

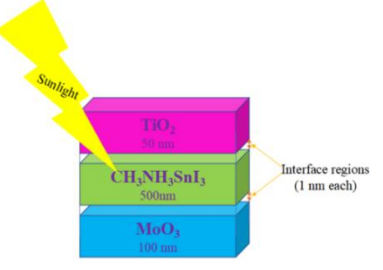

Fig. 1: Perovskite solar cell device structure: A 500 nm perovskite layer is stacked between 50 nm thick electron (TiO_2) and 100 nm hole (MoO_3) transport layer. 1 nm layers are added at the interface to account for interface properties within the drift–diffusion simulations.

[4]*Department of General Physics, Satbayev University, Almaty, 05013, Kazakhstan*

[*]*Email:* omarovazhansaya7@gmail.com (Zh. Omarova), y.merkibayev@satbayev.university (Y. Merkibayev)

2. Simulation model

We set-up a perovskite solar cell with a 500 nm $CH_3NH_3SnI_3$ photoactive layer, a 100 nm hole transport layer (HTL) and 50 nm electron transport layer (ETL) using TiO_2 and MoO_3 as ETL and HTL, respectively. We include 1 nm wide regions at the ETL/perovskite and HTL/perovskite interfaces,[55–58] in which material properties such as the conduction and valence bands as well as the dielectric constant are gradually varied using an effective medium approach.[53] The device structure is shown in Fig. 1.

The constant mobility model is employed for the perovskite and charge transport layers. Since the ions do not cross the charge transport layer, ionic mobility in the charge transport layer is considered to be zero. Charge and ionic transport within the device are governed by electrically induced drift and diffusion. The full set of equations reads as follows Eq. (2):

$$\begin{cases} \nabla\cdot(\epsilon\nabla\Phi) = -q\left(n - p + N_a^- - N_d^+ - N_{ct} + N_{an} + n_t^- - n_t^+\right) \\ \nabla\cdot\left\{\mu_n n(\nabla\Phi_n)\right\} = G - R_{dir} - R_{SRH} \\ \nabla\cdot\left\{\mu_p p(\nabla\Phi_p)\right\} = G - R_{dir} - R_{SRH} \\ \nabla\cdot\left\{\mu_{ct} N_{ct}\left(k_B T\frac{\partial N_{ct}}{\partial x}\right)\right\} = 0 \\ \nabla\cdot\left\{\mu_{an} N_{an}\left(k_B T\frac{\partial N_{an}}{\partial x}\right)\right\} = 0 \end{cases}, \quad (2)$$

The first equation solves the Poisson equation, and the final four equations are the continuity equations for the electrons (n), holes (p), cations (ct) and anions (an), respectively. ϵ is the material permittivity, Φ the electrostatic potential, and q is the elementary charge. n and p are the time-dependent electron and hole densities, respectively; N_{ct} and N_{an} represent the time-dependent cation and anion densities, respectively. N_d^+ and N_a^- label the ionized donor and ionized acceptor density, respectively. μ_n, μ_p, μ_{ct} and μ_{an} give the electron, hole, cation and anion mobilities, respectively. n_t^+ and n_t^- represent hole and electron trap concentrations, respectively. Φ_n and Φ_p are the electrochemical potentials of the electrons and the holes. All densities and potentials are a function of space and time. The model solves the continuity equations in time and position. For further details on the numerical solver, we refer to the publications of Calado *et al.*[53,55]

Direct (bimolecular) recombination of electrons and holes is included via R_{dir} Eq. (3):

$$R_{dir} = B(np - n_i^2), \quad (3)$$

where B is the bimolecular recombination rate constant, and n_i is the intrinsic carrier density. To include trapping of charge carriers by defects and the traps, we use the Shockley–Read–Hall recombination given by Eq. (4):[59,60]

$$R_{SRH} = \frac{np - n_i^2}{\left(n + N_c exp\left(\frac{E_t - E_c}{k_B T}\right)\right)\tau_p + \left(p + N_v exp\left(\frac{E_v - E_t}{k_B T}\right)\right)\tau_n}, \quad (4)$$

where E_t is the trap energy level, E_c and E_v label the conduction band minimum and valence band maximum, respectively. N_c and N_v are the effective density of states within the conduction and valence band respectively. τ_p and τ_n are the trapping times of holes and the electrons, respectively. Traps states are required to obtain hysteretic effects in the J–V characteristics.[55,56,61] Modeling without traps can result in J–V profiles with no hysteresis,[62] suggesting that the trapping might be one of the essential factors inducing the hysteresis. The trapping time is defined in terms of trap capturing coefficient Cn,p and the trap density as follows Eq. (4):

$$\tau_{n,p} = \frac{1}{N_t C_{n,p}}, \quad (4)$$

Higher trap density (N_t) implies a more efficient trapping and hence shorter trapping time $\tau_{n,p}$. Acceptor and donor traps are considered to be located in the middle of the bandgap. Recombination in the bulk is usually low, which explains the long diffusion lengths of charge carriers. Trapping times at the perovskite/ETL and perovskite/HTL interfaces are considered to be smaller than the bulk perovskite.

We apply a J–V scan as follows: First, the equilibrated solution at short-circuit condition without illumination is solved. Then, illumination is switched on, and the steady-state is calculated. After reaching a steady-state, we sweep the voltage with a constant scan rate until reaching the open-circuit voltage. Then, the sweep direction is reversed, and the simulation stops at the short-circuit condition. All parameters used for the drift–diffusion simulations are listed in Table 1.

Table 1: List of parameters used in drift–diffusion simulations. The asterisks (*) note that the listed value is varied during the simulations.

Perovskite parameters	Value	Units	Ref.
Valence band maximum	-5.47	eV	[64]
Conduction band minimum	-4.17	eV	[64]
Electron mobility	1.6	$cm^2/(V\ s)$	[65]
Hole mobility	1.6	$cm^2/(V\ s)$	[65]
Relative permittivity	8.2	–	[38]
Cation and anion density	1018	cm^{-3}	*
Cation mobility	10^{-12}	$cm^2/(V\ s)$	*
Anion mobility	10^{-12}	$cm^2/(V\ s)$	*
Bimolecular recombination rate	1×10^{-12}	$cm^{-3}\ s^{-1}$	[66]
Surface recombination velocity	1	$cm\ s^{-1}$	[66]
τ_n and τ_p in bulk perovskite	1×10^{-6}	S	[66]
Maximum optical generation rate	1.5×10^{22}	$cm^{-3}\ s^{-1}$	fit
MoO_3 parameters	Value	Units	Ref.
HOMO energy	−5.50	eV	[67]
LUMO energy	−2.50	eV	[67]
Relative permittivity	12.50	–	[67]
p-type doping	1×10^{18}	cm^{-3}	[67]
Hole mobility in MoO_3	100	$cm^2/(V\ s)$	[67]
TiO_2 parameters	Value	Units	Ref.
Bandgap	3.2	eV	[68]
Conduction band minimum	−4	eV	[68]
Relative permittivity	100	–	[69]
Electron mobility	6.0×10^{-3}	$cm^2/(V\ s)$	[69]
Contact parameters	Value	Units	Ref.
Anode Fermi level	−4.3	eV	fit
Cathode Fermi level	−5.3	eV	fit

3. Results and discussion

All simulations are performed using a voltage sweep rate of 20 mV s^{-1}.

Previous work by Futscher *et al.*[63] has demonstrated a three-order-of-magnitude disparity in diffusion coefficients between methylammonium (MA^+) and iodide (I^-) ions. In Ref.,[55] an ion mobility value of 10^{-12} cm^2 V^{-1} s^{-1} was employed. Drawing upon these findings, we adopt ionic mobilities of μ_{an}= 10^{-10}-10^{-14} $cm^2V^{-1}s^{-1}$ for the anion species and μ_{ct}=10^{-10}-10^{-14} $cm^2V^{-1}s^{-1}$ for the cation species.[55,63]

A comprehensive summary of all simulation parameters is provided in Table 1.

Fig. 2 presents the current density–voltage (J–V) characteristics measured in both forward (dashed line) and reverse (solid line) scan directions. The pristine perovskite device exhibits a short-circuit current density (J_{SC}) of 32.42 mA cm^{-2} and an open-circuit voltage (V_{OC}) of 1.05 V. With a fill factor (FF) of 0.78, this makes a power conversion efficiency (PCE) of 26.70 %. Note that the J–V-curves in the forward and backward direction of the neat device overlap as it shows no hysteresis.

Adding ions leads to hysteresis in the J–V-sweep with an HI of 0.039. The J_{SC} slightly decreases to 32.25 mA cm^{-2}, accompanied by a modest reduction in FF to 0.75. Meanwhile, the V_{OC} remains essentially unchanged at 1.07 V. As a result, the PCE declines to 25.92%. Despite the incorporation of substantial ionic densities, the corresponding degradation in device performance remains relatively limited.

It is important to highlight that experimental techniques typically estimate ionic densities in the range of 2.5×10^{16} cm^{-3} to 1×0^{18} cm^{-3}.[70] In contrast, theoretical models have suggested the possibility of significantly higher ionic concentrations, reaching up to 10^{19} cm^{-3}, particularly localized at grain boundaries or near the perovskite surface.[34,56,71–73]

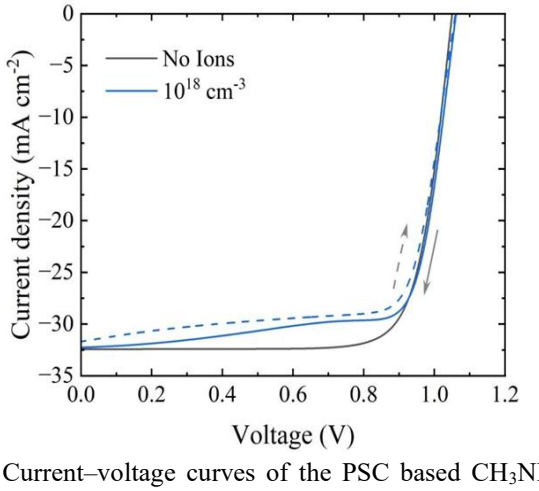

Fig. 2: Current–voltage curves of the PSC based $CH_3NH_3SnI_3$ devices with different ionic properties. The black curve shows the curve if no ions are considered. Blue curve shows simulations with an ion density of 10^{18} cm^{-3} for both the anions and cations. Dashed line shows the current density in forward and backward sweep direction, respectively. The arrows denote the sweep direction.

As the charge carrier density increases, bimolecular recombination between unbound electrons and holes becomes the dominant mechanism.[74] To elucidate the processes underlying bimolecular recombination, a proper separation of excitonic and continuum states is required. The bimolecular recombination rate constants are determined according to the Van Roosbroeck–Shockley relation,[75] which describes absorption processes involving electrons and holes both with and without accounting for Coulombic correlations.

Intense bimolecular recombination reduces the charge carrier diffusion length, necessitating an increased absorption coefficient to compensate, which in turn allows for a reduction in absorber layer thickness. This mechanism is particularly pronounced at low temperatures and low defect concentrations, making it a key factor in the development of high-quality materials.

As shown in Fig. 3, reducing the bimolecular recombination rate (from 10^{-8} to 10^{-11} $cm^3{\cdot}s^{-1}$) leads to an increase in V_{OC} up to 1.06 V and a reduction in hysteresis. At low recombination rates, hysteresis is diminished, indicating more stable device operation. The improvement in efficiency is attributed to reduced recombination losses. Minimizing undesirable recombination, particularly at interfaces, directly contributes to enhanced device performance and increased efficiency.

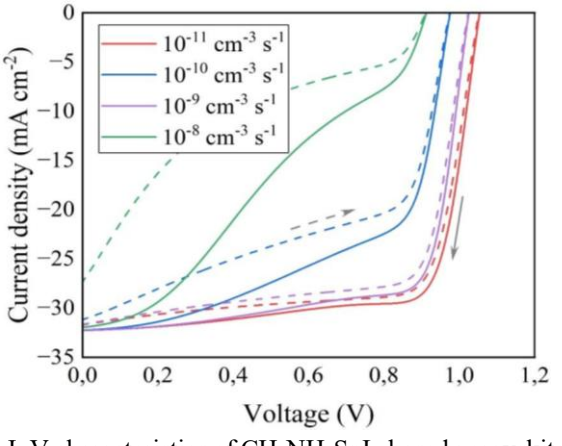

Fig. 3: J–V characteristics of $CH_3NH_3SnI_3$-based perovskite solar cells at different bimolecular recombination rates.

Table 2 presents the dependence of key photovoltaic parameters of the solar cell on the rate of bimolecular (including surface) charge carrier recombination. The analysis of the data demonstrates that a reduction in recombination rate has a favorable effect on device performance, improving all major efficiency metrics.

In particular, V_{OC} increases from 0.91 V to 1.05 V as the recombination rate decreases, indicating reduced energy losses during carrier transport across the heterojunction and a smaller thermodynamic deviation from the ideal case. The short-circuit current density J_{SC} also increases from 26.72 to 31.62 mA/cm², which can be attributed to reduced carrier losses prior to their collection at the electrodes. Accordingly, the fill factor (FF) shows a significant rise from 0.18 to 0.74, indicating a reduction in parasitic processes such as bulk and interfacial recombination, and more efficient operation of the internal

Table 2: Dependence of key photovoltaic parameters of the solar cell on the bimolecular recombination rate of charge carriers.

B ($cm^{-3}s^{-1}$)	V_{OC} (V)	J_{SC} (mA cm^{-2})	FF (-)	PCE (%)	HI
10^{-11}	1.05(1.06)	31.62(32.25)	0.74(0.75)	24.76(25.78)	0.039
10^{-10}	0.98(0.98)	32.02(32.22)	0.54(0.57)	16.44(18.12)	0.093
10^{-9}	1.02(1.04)	31.57(32.26)	0.73(0.73)	23.46(24.48)	0.041
10^{-8}	0.91(0.93)	26.72(31.90)	0.18(0.29)	4.32(8.44)	0.488

circuitry of the solar cell. Collectively, these improvements lead to a dramatic increase in the overall power conversion efficiency (PCE), by nearly sixfold—from 4.32% to 24.76%.

The hysteresis index (HI), which reflects the degree of instability in the output characteristics depending on the scan direction of the current-voltage curve, significantly decreases from 0.488 to 0.039. This indicates a stabilization of charge transport processes and a minimization of effects associated with ionic mobility and trap states at interfacial boundaries.

Thus, the reduction of the bimolecular recombination rate is a critical factor for enhancing both the performance and stability of next-generation solar cells.

Hysteresis in the current-voltage (J–V) characteristics of perovskite solar cells (PSCs) arises from the slow drift of ions within the photoactive layer. This effect becomes particularly pronounced in the presence of mobile ionic species, such as methylammonium (MA^+) and iodide (I^-), which redistribute under the influence of an electric field, creating spatial internal fields capable of significantly altering device behavior under varying measurement conditions. The present study examines the impact of voltage scan rate on the extent of hysteresis in J–V characteristics, taking into account bimolecular recombination.

Fig. 4(a) and (b) present the calculated J–V characteristics at different scan rates and bimolecular recombination coefficients of 10^{-10} $cm^3 \cdot s^{-1}$ and 10^{-12} $cm^3 \cdot s^{-1}$, respectively. In both cases, pronounced hysteresis is observed at low scan rates (below 10^{-9} $V \cdot s^{-1}$), which is attributed to the ability of ions to redistribute in response to changes in the external electric field, thereby generating an additional internal field that affects charge transport.

At a scan rate of 0.02 $V \cdot s^{-1}$, hysteresis is noticeable, which is attributed to the partial redistribution of ions within the device, forming localized internal fields that influence charge carrier extraction. As the scan rate increases to 0.04 $V \cdot s^{-1}$, the degree of hysteresis decreases, since the ions no longer fully respond to the voltage changes. At 0.1 $V \cdot s^{-1}$, hysteresis is significantly reduced, indicating an approach to the relaxation times of the ionic species, whereby the internal fields do not have sufficient time to fully develop.

At even higher scan rates, such as 1 $V \cdot s^{-1}$ and 5 $V \cdot s^{-1}$, the hysteresis effect becomes minimal or completely disappears. Under these conditions, the majority of ions remain effectively immobile, and their contribution to the variation of the internal potential within the device becomes negligible. This accounts for the more symmetric shape of the J–V curves and the absence of a pronounced difference between forward and reverse scans.

Thus, it can be concluded that the extent of hysteresis largely depends on the relationship between the ionic relaxation time and the rate of change of the external voltage. Slow scanning allows ions to follow the voltage and form internal fields, thereby enhancing hysteresis. In contrast, at fast scan rates, ions do not have sufficient time to redistribute, resulting in the suppression of hysteresis. Therefore, the choice of scan rate plays a critically important role in the accurate evaluation of the operational characteristics of perovskite solar cells. Employing excessively high scan rates may lead to an underestimation of the degree of instability and mask potential issues related to ionic mobility.

For a deeper understanding of the impact of recombination mechanisms on the extent of hysteresis, a comparative analysis was conducted between two models differing in their bimolecular recombination coefficient (B). The extracted hysteresis index (HI) values from all numerical simulations are presented in Table 3. At a high voltage scan rate of 5 $V \cdot s^{-1}$, the model with B = 10^{-10} $cm^3 \cdot s^{-1}$ exhibits a slight hysteresis with HI ≈ 9 × 10^{-4}. Meanwhile, when the bimolecular recombination coefficient is reduced to B = 10^{-12} $cm^3 \cdot s^{-1}$, HI decreases to 8 × 10^{-4}. A similar trend is observed at other investigated scan rates: in all cases, the model with the higher recombination coefficient shows significantly more pronounced hysteresis. Particularly noteworthy behavior is observed at the minimum scan rate of 0.02 $V \cdot s^{-1}$.

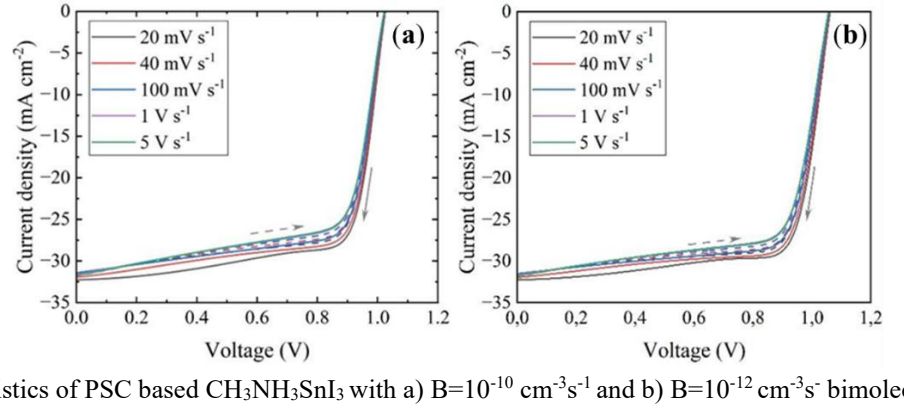

Fig. 4: J–V-characteristics of PSC based $CH_3NH_3SnI_3$ with a) B=10^{-10} $cm^{-3}s^{-1}$ and b) B=10^{-12} $cm^{-3}s^{-}$ bimolecular` recombination.

Table 3: Hysteresis index (HI) of the J–V-characteristics.

Scan rate (V s^{-1})	HI(B=10^{-10} $cm^{-3}s^{-1}$)	HI(B=10^{-12} $cm^{-3}s^{-1}$)
0.02	0.0414	0.0389
0.04	0.0371	0.0356
0.1	0.0249	0.0225
1	0.0041	0.0036
5	0.0009	0.0008

The current–voltage characteristics (J–V curves) of perovskite solar cells are closely dependent on the charge carrier lifetime (τ), which governs the efficiency of transport and recombination processes. An increased carrier lifetime facilitates more effective separation and transport of photogenerated carriers, minimizing recombination losses and thereby enabling high power conversion efficiency and stable device operation. In contrast, a reduced carrier lifetime leads to enhanced bulk and interfacial recombination, resulting in decreased short-circuit current density (J_{SC}) and open-circuit voltage (V_{OC}), increased hysteresis, and overall deterioration of the device's energy conversion efficiency.

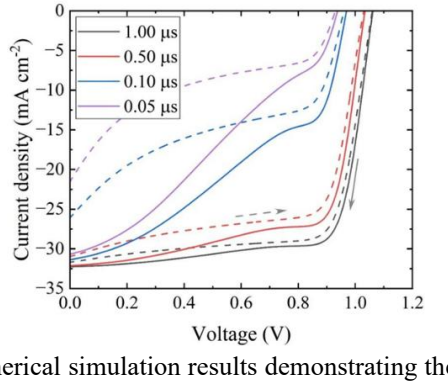

Fig. 5: Numerical simulation results demonstrating the influence of charge carrier lifetimes (τ_n, τ_p) on the performance characteristics of $CH_3NH_3SnI_3$-based perovskite solar cells (PSCs).

Fig. 5 presents the J–V curves for various charge carrier lifetimes. At τ = 1.00 μs, the maximum short-circuit current density is achieved, with J_{SC} = 31.62 mA/cm^2, and the difference between forward and reverse scans is minimal, indicating a low level of hysteresis and stable device operation. This behavior is characteristic of a solar cell with efficient charge extraction and minimal recombination losses.

However, when the carrier lifetime decreases to 0.10 μs—and especially to 0.05 μs—a sharp degradation of the device parameters is observed: J_{SC} drops to 25.64 mA/cm^2 and 20.87 mA/cm^2, respectively. The J–V curve becomes noticeably more sloped, particularly in the high-voltage region (0.8–1.0 V), indicating deteriorated diffusive transport and enhanced recombination. The gap between the forward and reverse scan branches becomes significantly more pronounced, reflecting increased hysteresis effects and growing instability in charge transport processes.

A reduction in carrier lifetime also negatively affects other key device parameters. According to the data presented in Table 4, the open-circuit voltage (V_{OC}) decreases from 1.07 V to 0.94 V as τ is reduced. Similarly, the fill factor (FF) drops from 0.74 to 0.27, indicating a deterioration in the shape of the J–V curve and increased losses. Collectively, these effects result in a nearly fivefold decrease in overall power conversion efficiency (PCE)—from 24.91% to 5.27%.

In addition, a significant increase in the hysteresis index (HI) is observed, confirming the degradation of device stability and the intensification of dynamic effects associated with slow internal processes such as ion migration and interfacial charge accumulation. Therefore, a long charge carrier lifetime is a critical parameter that determines both the efficiency and operational stability of perovskite solar cells.

Fig. 6 illustrates the simulated current density–voltage (J–V) characteristics of a perovskite solar cell for various electron (S_n) and hole (S_p) surface recombination velocities, where $S_n = S_p = 10^0$, 10^1, 10^2, and 10^3 cm/s. Both forward (solid lines) and reverse (dashed lines) voltage scans are shown, with the scan direction indicated by grey arrows. As seen in Fig. 6, at the lowest surface recombination velocities ($S_n = S_p = 10^0$ cm/s, black curves), the forward and reverse scans nearly overlap, indicating minimal hysteresis. This reflects efficient carrier extraction and negligible interfacial recombination losses.

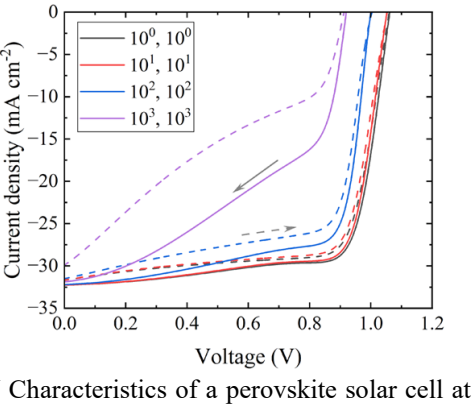

Fig. 6: J–V Characteristics of a perovskite solar cell at different electron (S_n) and Hole (S_p) surface recombination velocities.

Table 4: Impact of charge carrier lifetime on key parameters of $CH_3NH_3SnI_3$-based perovskite solar cells.

τ_n, τ_p (μs)	V_{OC} (V)	J_{SC} (mA cm^{-2})	FF (-)	PCE (%)	HI
1.00	1.07(1.07)	31.62(32.25)	0.74(0.75)	24.91(25.92)	0.039
0.50	1.04(1.04)	30.86(32.10)	0.68(0.70)	21.89(23.38)	0.063
0.10	0.97(0.98)	25.64(31.30)	0.40(0.39)	10.13(11.92)	0.150
0.05	0.93(0.94)	20.87(30.58)	0.27(0.31)	5.27(8.80)	0.401

When the surface recombination velocities increase to 10^1 cm/s (red curves), a slight deviation between the forward and reverse scans appears, indicating the onset of moderate hysteresis.

With a further increase to $S_n = S_p = 10^2$ cm/s (blue curves), the hysteresis becomes more pronounced. The reverse scan exhibits a higher current density than the forward scan over a wide voltage range, indicating delayed carrier recombination and interfacial charge accumulation effects.

The strongest hysteresis is observed at the highest recombination velocities ($S_n = S_p = 10^3$ cm/s, purple curves), where the forward scan exhibits a pronounced S-shaped distortion—an indication of poor interface quality and strong interfacial recombination. The significant divergence between the forward and reverse scans clearly reflects pronounced ionic and electronic coupling effects, leading to substantial device non-idealities.

These results confirm that increased surface recombination velocities significantly degrade diode quality and exacerbate hysteresis in perovskite solar cells. This is attributed to enhanced charge accumulation at interfaces, which alters the internal electric field and impedes efficient carrier transport. Moreover, the S-shaped behavior of the J–V curves at high recombination velocities suggests substantial screening of the built-in potential due to ionic redistribution, as previously reported in the literature.[76]

Therefore, effective passivation strategies to reduce surface recombination velocities are crucial for minimizing hysteresis and optimizing the overall photovoltaic performance of perovskite solar devices.

To investigate the impact of surface recombination processes on the performance of perovskite solar cells, we systematically varied the electron (S_n) and hole (S_p) surface recombination velocities from 10^0 to 10^3 cm/s. The resulting device parameters, including open-circuit voltage (V_{OC}), short-circuit current density (J_{SC}), fill factor (FF), power conversion efficiency (PCE), and hysteresis index (HI), were extracted from forward and reverse J–V scans and summarized in Table 5.

At the lowest surface recombination velocities ($S_n = S_p =$ 100 cm/s), the solar cell exhibits optimal performance with an open-circuit voltage (V_{OC}) of 1.07 V, a short-circuit current density (J_{SC}),) of 31.63 mA/cm² (forward scan), a fill factor (FF) of 0.74, and a corresponding power conversion efficiency (PCE) of 24.91%. The hysteresis index (HI) is minimal at 0.0389, indicating negligible hysteresis in the J–V characteristics.

With an increase in S_n and S_p to 10^1 cm/s, a slight decline in device performance is observed. The open-circuit voltage (V_{OC}) remains at 1.07 V, while the short-circuit current density (J_{SC}) remains relatively stable. However, the fill factor (FF) decreases slightly to 0.73, and the power conversion efficiency (PCE) drops to 24.57%. The hysteresis index (HI) increases modestly to 0.0405, suggesting a mild increase in hysteresis behavior due to enhanced surface recombination. With a further increase in recombination velocities to 10^2 cm/s, degradation becomes more pronounced. V_{OC} decreases to 1.01 V, and FF falls to 0.68. Although J_{SC} remains relatively high, the overall PCE declines to 21.66%. The hysteresis index rises significantly to 0.0676, indicating a stronger asymmetry between the forward and reverse J–V curves.

At the highest tested recombination velocity ($S_n = S_p = 10^3$ cm/s), significant performance losses are observed. The open-circuit voltage (V_{OC}) drops to 0.93 V, the short-circuit current density (J_{SC}) decreases to 29.64 mA/cm², and the fill factor

(FF) sharply declines to 0.30. This results in a substantial reduction of the power conversion efficiency (PCE) to only 8.24%. Notably, the hysteresis index (HI) reaches 0.3727, indicating pronounced hysteresis and highlighting significant charge trapping effects at the interface as well as ion accumulation.

These results underscore the critical importance of controlling surface recombination at the interfaces between the perovskite absorber and transport layers. High surface recombination velocities increase carrier losses at the interfaces, which not only reduce V_{OC}, J_{SC} and FF but also exacerbate hysteresis phenomena due to enhanced charge trapping and slowed ionic relaxation. Therefore, minimizing S_n and S_p through effective interface engineering and surface passivation is essential for achieving high performance and stable operation of perovskite solar cells.

Ionic defect mobility significantly influences the current–voltage (J–V) characteristics of perovskite solar cells (PSCs). In this final section, we investigate the effects of varying cationic and anionic mobilities on the J–V behavior and the degree of hysteresis in $CH_3NH_3SnI_3$-based PSCs. The cation activation energy, ionic defect density, and voltage scan rate are held constant at 0.1 eV, 10^{18} cm^{-3}, and 20 $mV \cdot s^{-1}$, respectively. The corresponding J–V curves are presented in Fig. 7.

Table 5: Effect of Electron (S_n) and Hole (S_p) surface recombination velocities on the performance parameters of PSC based on $CH_3NH_3SnI_3$.

S_n and S_p (cm/s)	V_{OC} (V)	J_{SC} (mA cm^{-2})	FF (-)	PCE (%)	HI
10^0	1.07(1.07)	31.63(32.25)	0.74(0.75)	24.91(25.92)	0.0389
10^1	1.07(1.05)	31.61(32.24)	0.73(0.75)	24.57(25.60)	0.0405
10^2	1.01(1.01)	31.42(32.19)	0.68(0.71)	21.66(23.23)	0.0676
10^3	0.93(0.93)	29.64(31.84)	0.30(0.46)	8.24(13.14)	0.3727

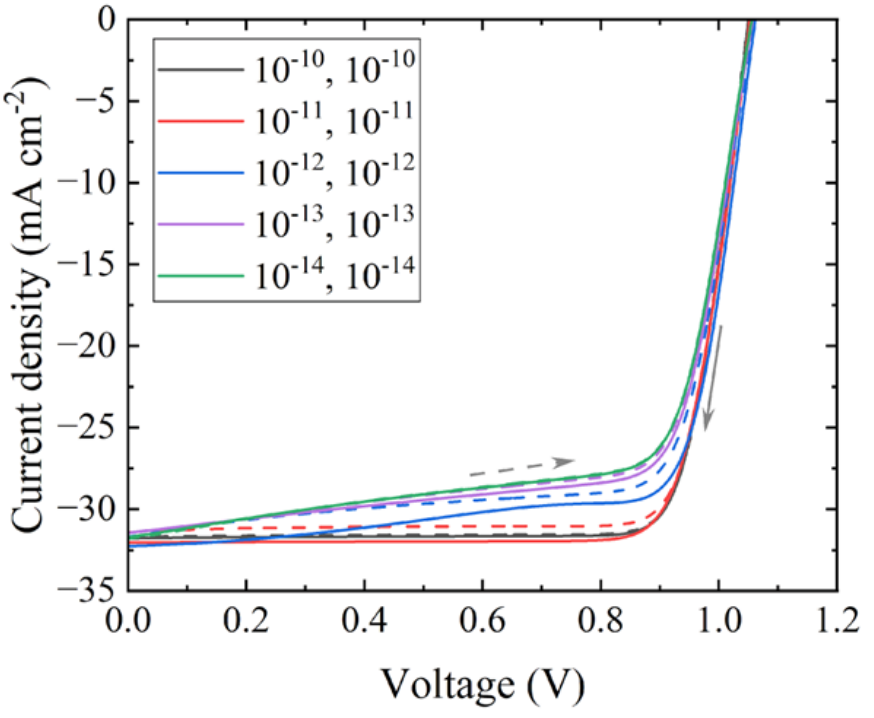

Fig. 7: Current–voltage (J–V) curves of $MAPbI_3$ devices with varying ionic mobilities μ = (μ_{an}, μ_{ct}): (a) both anion and cation mobilities varied simultaneously; (b) anion mobility varied while cation mobility is fixed at 1 × 10^{-12} cm^2 V^{-1} s^{-1}. Mobility values are given in cm^2 V^{-1} s^{-1}. Dashed and solid lines represent the current density during forward and backward voltage sweeps, respectively. Arrows indicate the direction of the voltage scan.

Table 6: Device parameters in forward (backward) direction for different ionic mobility μ_{an}, μ_{ct} (in units $cm^2V^{-1}s^{-1}$). The open-circuit voltage is equal for both the forward and backward direction.

μ_{an}, μ_{ct}	V_{OC} (V)	J_{SC} (mA cm^{-2})	FF (-)	PCE (%)	HI
10^{-10}, 10^{-10}	1.05(1.05)	31.68(31.77)	0.82(0.82)	27.36(27.42)	0.002
10^{-11}, 10^{-11}	1.06(1.05)	31.40(32.04)	0.80(0.81)	26.92(27.38)	0.017
10^{-12}, 10^{-12}	1.07(1.07)	31.63(32.25)	0.74(0.75)	24.91(25.92)	0.039
10^{-13}, 10^{-13}	1.07(1.07)	31.74(31.41)	0.71(0.72)	23.92(24.26)	0.014
10^{-14}, 10^{-14}	1.07(1.07)	31.75(31.66)	0.70 (0.70)	23.68(23.72)	0.002

The initial simulation was conducted with equal ionic mobilities for both anions and cations, set at μ_{an} = μ_{ct} = 10^{-10} cm^2 V^{-1} s^{-1}. At this relatively high mobility, ions migrate rapidly during voltage sweeps, effectively mitigating charge accumulation at interfaces and thereby suppressing observable hysteresis. However, the open-circuit voltage (V_OC) is limited to 1.05 V, attributed to enhanced electron trapping linked to the mobile cationic species.

As ionic mobility is reduced, hysteresis becomes increasingly apparent, as illustrated in Fig. 7. A detailed summary of the photovoltaic performance metrics—including V_{OC}, short-circuit current density (J_{SC}), fill factor (FF), and power conversion efficiency (PCE)—under both forward and reverse scan conditions is provided in Table 6. Across the studied mobility range (10^{-14} cm^2 V^{-1} s^{-1} to 10^{-10} cm^2 V^{-1} s^{-1}), V_{OC} shows only a marginal increase from 1.05 V to 1.07 V, and J_{SC} remains nearly constant, varying slightly from 31.68 mA cm^{-2} to 31.75 mA cm^{-2}.

The most notable effect of decreasing ionic mobility is observed in the hysteresis index (HI), which increases substantially, along with reductions in FF and overall PCE. These findings are consistent with previous literature reports.[49,73,77,78] Specifically, for μ_{an}=μ_{ct}=10^{-12} cm^2 V^{-1} s^{-1}, pronounced hysteresis is observed, characterized by an HI of 0.039. Under these conditions, the PCE drops to 24.91% during the forward scan and 25.92% during the reverse scan.

These results underscore the critical role of ionic defect mobility in dictating the dynamic performance and operational stability of perovskite solar cells, highlighting the need for precise control over ionic behavior in device engineering.

4. Conclusion

This study systematically investigates the influence of various recombination mechanisms, ionic effects, and measurement conditions on the current–voltage (J–V) characteristics and performance of perovskite solar cells (PSCs). The analysis reveals that the presence of mobile ionic species induces hysteresis, although moderate ionic densities exert a relatively limited impact on the overall power conversion efficiency (PCE). However, key device parameters—including short-

circuit current density (J_{SC}), open-circuit voltage (V_{OC}), and fill factor (FF)—are strongly dependent on the bimolecular recombination rate and carrier lifetime.

A principal finding is the strong correlation between reduced bimolecular recombination rates and enhanced photovoltaic performance. Lower recombination rates lead to improved charge extraction, increased V_{OC} and J_{SC}, and a significant reduction in the hysteresis index (HI), thereby enabling more stable and efficient device operation. Moreover, extended carrier lifetimes result in marked improvements across all critical photovoltaic parameters, underscoring their role in minimizing recombination losses and enhancing device stability.

The modeling also demonstrates that hysteresis in J–V characteristics is primarily governed by the interplay between ionic relaxation times and voltage scan rates. Slow scan rates permit ion redistribution and the formation of internal fields, which amplify hysteresis, whereas fast scan rates suppress ionic migration effects, minimizing hysteresis and revealing more intrinsic device behavior. Furthermore, elevated surface recombination velocities at charge transport interfaces significantly degrade device performance and exacerbate hysteresis, with pronounced S-shaped distortions observed at high recombination rates.

Overall, these results highlight the critical importance of controlling recombination dynamics, ion migration, and interfacial properties to optimize both efficiency and operational stability of PSCs. Accurate measurement protocols and effective passivation strategies are essential for mitigating hysteresis and achieving high-performance perovskite photovoltaic technologies of the next generation.

Acknowledgments

These studies have been carried out with the financial support of the Ministry of Science and Higher Education of the Republic of Kazakhstan under grant AP19174728. Funding: This research was funded by the Science Committee of the Ministry of Science and Higher Education of the Republic of Kazakhstan (Grants No. AP19174728).

Conflict of Interest

There is no conflict of interest.

Supporting Information

Not applicable.

CRediT Statement

Zhansaya Omarova: Writing - Original draft, Writing - Review and editing, Methodology, Investigation, Validation, Formal analysis, Conceptualization, Project administration, Funding acquisition. **Yerik Merkibayev:** Methodology, Investigation, Formal analysis, Resources. **Bauyrzhan Bazarbay:** Software, Formal analysis, Conceptualization, Resources. **Ramina Shumakova:** Software, Formal analysis, Conceptualization, Resources. **Erik Shalenov:** Writing - Review and editing, Methodology, Investigation, Formal analysis, Validation, Conceptualization, Supervision.

References

[1] S. Bellani, A. Bartolotta, A. Agresti, G. Calogero, G. Grancini, A. Di Carlo, E. Kymakis, F. Bonaccorso, Solution-processed two-dimensional materials for next-generation photovoltaics, *Chemical Society Reviews*, 2021, **50**, 11870-11965, doi: 10.1039/d1cs00106j.

[2] R. Guchhait, B. Sarkar, Increasing growth of renewable energy: a state of art, *Energies*, 2023, **16**, 2665, doi: 10.3390/en16062665.

[3] Z. Wang, X. Chen, A. Sun, L. Liu, Y. Chen, L. Hu, D. Zhang, H. Ren, Y. Liu, J. Shi, B. Yu, G. Hou, P. Yang, Y. Zhao, X. Zhang, Zinc-tin oxide transparent conductive layers *via* reactive plasma deposition for silicon heterojunction solar cells, *Solar Energy Materials and Solar Cells*, 2025, **293**, 113835, doi: 10.1016/j.solmat.2025.113835.

[4] Best Research-Cell Efficiency Chart Available online: https://www.nrel.gov/pv/cell-efficiency.html.

[5] J. Park, J. Kim, H.-S. Yun, M. J. Paik, E. Noh, H. J. Mun, M. G. Kim, T. J. Shin, S. I. Seok, Controlled growth of perovskite layers with volatile alkylammonium chlorides, *Nature*, 2023, **616**, 724-730, doi: 10.1038/s41586-023-05825-y.

[6] J. You, Q. Gao, J. Wang, W. Jiao, J. Zhu, Z. Gao, Y. Luo, J. Qu, C. Ding, W. Wang, F. Li, X. He, Q. Song, X. Lang, C. Xiao, C. Chen, D. Zhao, Crystallization control and interface passivation for efficient hole transport layer-free and methylammonium-free low-bandgap tin-lead perovskite solar cells, *Nano Energy*, 2025, **142**, 111209, doi: 10.1016/j.nanoen.2025.111209.

[7] X. Zeng, Q. Luo, J. Li, Y. Li, W. Wang, Y. Li, R. Wu, D. Pan, G. Song, J. Li, Z. Guo, N. Wang, A multifunctional pentlandite counter electrode toward efficient and stable sensitized solar cells, *Advanced Composites and Hybrid Materials*, 2021, **4**, 392-400, doi: 10.1007/s42114-021-00233-0.

[8] G. Nazir, A. Rehman, J. Gautam, M. Ikram, S. Hussain, S. Aftab, K. Heo, S.-Y. Lee, S.-J. Park, Advancements in flexible Perovskite solar cells and their integration into self-powered wearable optoelectronic systems, *Advanced Powder Materials*, 2025, **4**, 100304, doi: 10.1016/j.apmate.2025.100304.

[9] S. Orecchio, D. Amorello, A. Contino, G. Maccarrone, A. Giuffrida, S. Orecchio, T. Fiore, I. Pibiri, D. Ricci, B. Pignataro, S. Barreca, G. Arrabito, Shielding the environment: Perfluoroalkylated pyrenes prevent lead leakage from perovskite solar cell, *Journal of Environmental Chemical Engineering*, 2025, **13**, 118098, doi: 10.1016/j.jece.2025.118098.

[10] P. Dissanayake, M. T. Hoang, S. Senanayake, W.-H. Chiu, W. Martens, D.-C. Qi, M. Klein, A. K. Pandey, Y. Yang, H. Wang, Parafilm-assisted fabrication of flexible perovskite solar cells to improve efficiency, *Solar Energy Materials and Solar Cells*, 2025, **293**, 113826, doi: 10.1016/j.solmat.2025.113826.

[11] A. Bakar, M. Ahmed, Z. B. Omarova, G. K. Toleubay, E. O. Shalenov, Revealing the improved elasto-mechanical, opto-electronic, thermodynamic and thermoelectric properties of double perovskites Rb_2TlAF6(a = Ir, Rh): a DFT analysis, *Surfaces and Interfaces*, 2025, **71**, 106777, doi: 10.1016/j.surfin.2025.106777.

[12] M. Ahmed, A. Bakar, A. Orynbassar, N. Shynarbek, M.A. Tahir, E.O. Shalenov, A.A. Ibraheem, First principles investigations of Lithium based hydrides LiXH 3(X=Al, Ga, In) for hydrogen storage applications, *International Journal of Hydrogen Energy*, 2025, **98**, 25–34, doi: 10.1016/j.ijhydene.2024.11.409.

[13] A. G. Kakimov, Y. Yerlanuly, A. Akhanuly, I. T. Dossayev, E. O. Shalenov, Z. T. Sadirkhanov, K. N. Dzhumagulova, A. Ng, A. N. Jumabekov, Passivation of perovskite layer surface states with pyridine in flexible and printed perovskite solar cells, *Flexible and Printed Electronics*, 2022, **7**, 035012, doi: 10.1088/2058-8585/ac8753.

[14] H. Muhammad, A. Bakar, A. Afaq, E. O. Shalenov, H. E. Ali, First principles investigations on physical properties and phonon-mediated superconductivity in CsTaC, *Radiation Physics and Chemistry*, 2026, **238**, 113178, doi: 10.1016/j.radphyschem.2025.113178.

[15] A. Bakar, M. Ahmed, Y. Khairy, E. O. Shalenov, M. M. Seisembayeva, K. N. Dzhumagulova, Structural, elastic, mechanical, electronic and optical properties of $${{{{\text{TlSnX}}}}}_3\, ({{\text{X}}}={{\text{Cl}}}, {{\text{Br}}}, {{\text{I}}})$$for sustainable energy applications, *Journal of Inorganic and Organometallic Polymers and Materials*, 2025, **35**, 166-186, doi: 10.1007/s10904-024-03269-z.

[16] M. Ahmed, A. Bakar, O. S. Erik, S. M. Madina, K. N. Dzhumagulova, A. Quader, A first-principles investigations of Lead-free SbPCa3 inverse perovskite for structural, electronic and optical properties with different DFT methods, *Physica B: Condensed Matter*, 2024, **690**, 416250, doi: 10.1016/j.physb.2024.416250.

[17] D. Abdullah, D. C. Gupta, Analyzing the structural, optoelectronic, and thermoelectric properties of InGeX3 (X = Br) perovskites *via* DFT computations, *Scientific Reports*, 2024, **14**, 23575, doi: 10.1038/s41598-024-72745-w.

[18] R. K. Pingak, S. Bouhmaidi, A. Harbi, L. Setti, F. Nitti, M. Moutaabbid, A. Z. Johannes, N. U. J. Hauwali, M. Z. Ndii, A DFT investigation of lead-free $TlSnX_3$ (X = Cl, Br, or I) perovskites for potential applications in solar cells and thermoelectric devices, *RSC Advances*, 2023, **13**, 33875-33886, doi: 10.1039/d3ra06685a.

[19] S. Paul, S. Mondal, S. Bera, A. Saha, R. Mishra, A. Majumder, M. K. Mandal, S. Roy, Synthesis, characterization, and density functional theory calculation studies of a novel Rb-based lead halide perovskite material, *Chemistry of Inorganic Materials*, 2023, **1**, 100015, doi: 10.1016/j.cinorg.2023.100015.

[20] T. Das, G. Di Liberto, G. Pacchioni, Density functional theory estimate of halide perovskite band gap: when spin orbit coupling helps, *The Journal of Physical Chemistry C*, 2022, **126**, 2184-2198, doi: 10.1021/acs.jpcc.1c09594.

[21] A. Akhanuly, I. T. Dossyaev, E. O. Shalenov, C. Valagiannopoulos, K. N. Dzhumagulova, A. Ng, A. N. Jumabekov, Modeling and comparative performance analysis of perovskite solar cells with planar or nanorod Sn_{O2} electron-transport layers, *Physical Review Applied*, 2023, **19**, 054039, doi: 10.1103/physrevapplied.19.054039.

[22] Q. Zhang, Q. Zhao, H. Wang, Y. Yao, L. Li, Y. Wei, R. Xu, C. Zhang, E. O. Shalenov, Y. Tu, K. Wang, M. Xiao, Tuning isomerism effect in organic bulk additives enables efficient and stable perovskite solar cells, *Nano-Micro Letters*, 2025, **17**, 107, doi: 10.1007/s40820-024-01613-z.

[23] M. S. Kiani, H. P. Parkhomenko, M. Mangrulkar, S. Aigarayeva, A. Akhanuly, E. O. Shalenov, A. Ng, A. N. Jumabekov, Stepping toward portable optoelectronics with SnO_2 quantum dot-based electron transport layers, *ACS Omega*, 2023, **8**, 21212-21222, doi: 10.1021/acsomega.3c02341.

[24] I. T. Dossayev, A. Akhanuly, H. P. Parkhomenko, K. N. Dzhumagulova, A. Ng, E. O. Shalenov, A. N. Jumabekov, Computer simulation and performance analysis of metal–semiconductor–metal back-contact perovskite solar cells, *Journal of Computational Electronics*, 2025, **24**, 85, doi: 10.1007/s10825-025-02326-1.

[25] H. P. Parkhomenko, E. O. Shalenov, Z. Umatova, K. N. Dzhumagulova, A. N. Jumabekov, Fabrication of flexible quasi-interdigitated back-contact perovskite solar cells, *Energies*, 2022, **15**, 3056, doi: 10.3390/en15093056.

[26] Y.-S. Jeon, D.-H. Kang, J.-H. Kim, N.-G. Park, Stability and efficiency improvement of perovskite solar cells by surface hydroxyl defect passivation of SnO_2 layer with 4-fluorothiophenol, *Journal of Materials Chemistry A*, 2023, **11**, 3673-3681, doi: 10.1039/d2ta08488k.

[27] S. AL-Shujaa, P. Zhao, D. He, B. Al-Anesi, Y. Feng, J. Xia, B. Zhang, Y. Zhang, Improving the efficiency and stability of perovskite solar cells by refining the perovskite-electron transport layer interface and shielding the absorber from UV effects, *ACS Applied Materials & Interfaces*, 2024, **16**, 28493-28504, doi: 10.1021/acsami.4c03329.

[28] L. Sun, T. Wang, Y. Wang, G. Li, Z. Deng, S. Sun, H. Tan, X. Wang, J. Chen, L. Peng, X. Liu, J. Lin, H. Li, Enhanced performance and stability of perovskite solar cells through modification of SnO_2 electron transport layer with stable conformation surfactant, *Advanced Energy Materials*, 2025, **15**, 2405581, doi: 10.1002/aenm.202405581.

[29] M. Khalifa, M. Dkhili, S. Aouida, H. Ezzaouia, Optimizing electron transport layers for high-efficiency perovskite solar cells using impedance spectroscopy, *Solar Energy Materials and Solar Cells*, 2024, **278**, 113196, doi: 10.1016/j.solmat.2024.113196.

[30] S. Gao, J.-J. Bae, D. S. Lee, T.-Y. Yang, S. S. Shin, Toward sustainable perovskite solar cells: from lead-free materials to environmental concerns and mitigation strategies, *EcoMat*, 2025, **7**, e70001, doi: 10.1002/eom2.70001.

[31] M. Tripathi, V. Vaibhav Mishra, B. S. Sengar, A. V. Ullas, Lead-free perovskite solar cell byUsing SCAPS-1D: Design and simulation, *Materials Today: Proceedings*, 2022, **62**, 4327-4331, doi: 10.1016/j.matpr.2022.04.832.

[32] M. F. Hossain, M. M. Rahman, M. Harun-Or-Rashid, M. Amami, L. Ben Farhat, M. F. Rahman, Probing the impact of four BSF layers on $MASnI_3$-based lead-free perovskite solar cells for >33% efficiency, *Advanced Theory and Simulations*, 2025, **8**, 2400662, doi: 10.1002/adts.202400662.

[33] M. N. Nahid, M. S. Shah, H. Mamur, R. Hosen, M. R. A.

Bhuiyan, Optimizing lead-free CH_3NH_3SnI3 perovskite solar cells by using SCAPS-1D software, *Chemistry of Inorganic Materials*, 2024, **4**, 100069, doi: 10.1016/j.cinorg.2024.100069.
[34] I. Ahmed, K. Prakash, S. M. Mobin, Lead-free perovskites for solar cell applications: recent progress, ongoing challenges, and strategic approaches, *Chemical Communications*, 2025, **61**, 6691-6721, doi: 10.1039/d4cc06835a.
[35] Z. Omarova, Performance simulation of eco-friendly solar cells based $ONCH_3NH_3SnI3$, *Eurasian Physical Technical Journal*, 2022, **19**, 58-64, doi: 10.31489/2022no2/58-64.
[36] Z. Omarova, D. Yerezhep, A. Aldiyarov, N. Tokmoldin, In silico investigation of the impact of hole-transport layers on the performance of CH_3NH_3SnI3 perovskite photovoltaic cells, *Crystals*, 2022, **12**, 699, doi: 10.3390/cryst12050699.
[37] Q. A. Alsulami, R. Al Foysal Redoy, S. Wageh, Efficiency optimization of lead-free $CH_3NH_3SnI_3^-$ based perovskite solar cells through material and structural modifications, *Scientific Reports*, 2025, **15**, 13170, doi: 10.1038/s41598-025-95473-1.
[38] P. K. Patel, Device simulation of highly efficient eco-friendly CH_3NH_3SnI3 perovskite solar cell, *Scientific Reports*, 2021, **11**, 3082, doi: 10.1038/s41598-021-82817-w.
[39] M. Mottakin, K. Sobayel, D. Sarkar, H. Alkhammash, S. Alharthi, K. Techato, M. Shahiduzzaman, N. Amin, K. Sopian, M. Akhtaruzzaman, Design and modelling of eco-friendly $CH_3NH_3SnI_3^-$Based perovskite solar cells with suitable transport layers, *Energies*, 2021, **14**, 7200, doi: 10.3390/en14217200.
[40] M. Lazemi, S. Asgharizadeh, S. Bellucci, A computational approach to interface engineering of lead-free $CH_3NH_3SnI_3$ highly-efficient perovskite solar cells, *Physical Chemistry Chemical Physics*, 2018, **20**, 25683-25692, doi: 10.1039/c8cp03660h.
[41] H.-J. Du, W.-C. Wang, J.-Z. Zhu, Device simulation of lead-free $CH_3NH_3SnI_3$perovskite solar cells with high efficiency, *Chinese Physics B*, 2016, **25**, 108802, doi: 10.1088/1674-1056/25/10/108802.
[42] M. Kari, K. Saghafi, Current-Voltage Hysteresis Reduction of CH3NH3PbI3 Planar Perovskite Solar Cell by Multi-Layer Absorber, *Micro and Nanostructures*, 2022, **165**, 207207, doi: 10.1016/j.micrna.2022.207207.
[43] J. Duan, Q. Yue, Q. Xiong, L. Wang, L. Zhu, K. Zhang, J. Zhang, H. Wang, Surface modification of SnO_2 blocking layers for hysteresis elimination of MAPbI3 photovoltaics, *Applied Surface Science*, 2019, **470**, 613-621, doi: 10.1016/j.apsusc.2018.11.163.
[44] W. Veurman, J. Kern, L. Pflüger, H. Wagner-Mohnsen, M. Müller, P. P. Altermatt, Z. Lou, M. Stolterfoht, F. Haase, S. Kajari-Schröder, R. Peibst, Deciphering hysteresis in perovskite solar cells: Insights from device simulations distinguishing shallow traps from mobile ions, *Solar Energy*, 2024, **284**, 113037, doi: 10.1016/j.solener.2024.113037.
[45] M. Minbashi, E. Yazdani, Comprehensive study of anomalous hysteresis behavior in perovskite-based solar cells, *Scientific Reports*, 2022, **12**, 14916, doi: 10.1038/s41598-022-19194-5.
[46] A. Singh, W. Kaiser, A. Gagliardi, Role of cation-mediated recombination in perovskite solar cells, *Solar Energy Materials and Solar Cells*, 2021, **221**, 110912, doi: 10.1016/j.solmat.2020.110912.
[47] Y. Yerlanuly, E. O. Shalenov, H. P. Parkhomenko, M. S. Kiani, Z. Kukhayeva, A. Ng, A. N. Jumabekov, Elucidating the hysteresis effect in printed flexible perovskite solar cells with SnO_2 quantum dot- and PCBM-based electron transport layers, *Heliyon*, 2024, **10**, e39667, doi: 10.1016/j.heliyon.2024.e39667.
[48] T. P. Schneider, J. Glaser, J. Horn, F. Schmitz, T. Gatti, D. Schlettwein, Transformation of polarization mechanisms by dimensional reduction in lead-free silver bismuth bromide double-perovskite thin films, *ACS Applied Electronic Materials*, 2024, **6**, 987-997, doi: 10.1021/acsaelm.3c01451.
[49] W. Tress, N. Marinova, T. Moehl, S. M. Zakeeruddin, M. K. Nazeeruddin, M. Grätzel, Understanding the rate-dependent J–V hysteresis, slow time component, and aging in $CH_3NH_3PbI_3$ perovskite solar cells: the role of a compensated electric field, *Energy & Environmental Science*, 2015, **8**, 995-1004, doi: 10.1039/c4ee03664f.
[50] T. Noma, D. Taguchi, T. Manaka, M. Iwamoto, Study of I-V hysteresis of tin perovskite solar cells using capacitance-voltage measurement coupled with charge modulation spectroscopy, *Molecular Crystals and Liquid Crystals*, 2019, **686**, 92-98, doi: 10.1080/15421406.2019.1648042.
[51] W. Ayaydah, E. Raddad, Z. Hawash, Sn-based perovskite solar cells towards high stability and performance, *Micromachines*, 2023, **14**, 806, doi: 10.3390/mi14040806.
[52] L. Huerta Hernandez, L. Lanzetta, A. M. Kotowska, I. Yavuz, N. Kalasariya, B. Vishal, M. Gibert-Roca, M. Piggott, D. J. Scurr, S. De Wolf, M. Stolterfoht, D. Baran, Deciphering the interplay between tin vacancies and free carriers in the ion transport of tin-based perovskites, *Energy & Environmental Science*, 2025, **18**, 4787-4799, doi: 10.1039/d5ee00632e.
[53] P. Calado, I. Gelmetti, B. Hilton, M. Azzouzi, J. Nelson, P. R. F. Barnes, Driftfusion: an open source code for simulating ordered semiconductor devices with mixed ionic-electronic conducting materials in one dimension, *Journal of Computational Electronics*, 2022, **21**, 960-991, doi: 10.1007/s10825-021-01827-z.
[54] S. N. Habisreutinger, N. K. Noel, H. J. Snaith, Hysteresis index: a figure without merit for quantifying hysteresis in perovskite solar cells, *ACS Energy Letters*, 2018, **3**, 2472-2476, doi: 10.1021/acsenergylett.8b01627.
[55] P. Calado, A. M. Telford, D. Bryant, X. Li, J. Nelson, B. C. O′ Regan, P. R. F. Barnes, Evidence for ion migration in hybrid perovskite solar cells with minimal hysteresis, *Nature Communications*, 2016, **7**, 13831, doi: 10.1038/ncomms13831.
[56] T. S. Sherkar, C. Momblona, L. Gil-Escrig, J. Ávila, M. Sessolo, H. J. Bolink, L. J. A. Koster, Recombination in perovskite solar cells: significance of grain boundaries, interface traps, and defect ions, *ACS Energy Letters*, 2017, **2**, 1214-1222, doi: 10.1021/acsenergylett.7b00236.
[57] H. Mehdizadeh-Rad, F. Mehdizadeh-Rad, F. Zhu, J. Singh, Heat mitigation in perovskite solar cells: The role of grain boundaries, *Solar Energy Materials and Solar Cells*, 2021, **220**,

110837, doi: 10.1016/j.solmat.2020.110837.
[58] A. Singh, A. Gagliardi, Efficiency of all-perovskite two-terminal tandem solar cells: a drift-diffusion study, *Solar Energy*, 2019, **187**, 39-46, doi: 10.1016/j.solener.2019.05.006.
[59] W. Shockley, W. T. Read, Statistics of the recombinations of holes and electrons, *Physical Review*, 1952, **87**, 835-842, doi: 10.1103/physrev.87.835.
[60] T. Nakamura, M. Imaizumi, H. Akiyama, Y. Okada, Practical target values of Shockley–Read–Hall recombination rates in state-of-the-art triple-junction solar cells for realizing conversion efficiencies within 1% of the internal radiative limit, *Progress in Photovoltaics: Research and Applications*, 2020, **28**, 417-424, doi: 10.1002/pip.3251.
[61] S. van Reenen, M. Kemerink, H. J. Snaith, Modeling anomalous hysteresis in perovskite solar cells, *The Journal of Physical Chemistry Letters*, 2015, **6**, 3808-3814, doi: 10.1021/acs.jpclett.5b01645.
[62] T. S. Sherkar, C. Momblona, L. Gil-Escrig, H. J. Bolink, L. J. A. Koster, Improving perovskite solar cells: insights from a validated device model, *Advanced Energy Materials*, 2017, **7**, 1602432, doi: 10.1002/aenm.201602432.
[63] M. H. Futscher, J. M. Lee, L. McGovern, L. A. Muscarella, T. Wang, M. I. Haider, A. Fakharuddin, L. Schmidt-Mende, B. Ehrler, Quantification of ion migration in $CH_3NH_3PbI_3$ perovskite solar cells by transient capacitance measurements, *Materials Horizons*, 2019, **6**, 1497-1503, doi: 10.1039/c9mh00445a.
[64] H. Wilhelm, H.-W. Schock, R. Scheer, Interface recombination in heterojunction solar cells: Influence of buffer layer thickness, *Journal of Applied Physics*, 2011, **109**, 084514, doi: 10.1063/1.3554409.
[65] N. K. Noel, S. D. Stranks, A. Abate, C. Wehrenfennig, S. Guarnera, A.-A. Haghighirad, A. Sadhanala, G. E. Eperon, S. K. Pathak, M. B. Johnston, A. Petrozza, L. M. Herz, H. J. Snaith, Lead-free organic–inorganic tin halide perovskites for photovoltaic applications, *Energy & Environmental Science*, 2014, **7**, 3061-3068, doi: 10.1039/c4ee01076k.
[66] T. Kirchartz, J. A. Márquez, M. Stolterfoht, T. Unold, Photoluminescence-based characterization of halide perovskites for photovoltaics, *Advanced Energy Materials*, 2020, **10**, 1904134, doi: 10.1002/aenm.201904134.
[67] M. M. Khatun, A. Hosen, S. R. Al Ahmed, Evaluating the performance of efficient $Cu_2NiSnS4$ solar cell: a two stage theoretical attempt and comparison to experiments, *Heliyon*, 2023, **9**, e20603, doi: 10.1016/j.heliyon.2023.e20603.
[68] P. Tiwana, P. Docampo, M. B. Johnston, H. J. Snaith, L. M. Herz, Electron mobility and injection dynamics in mesoporous ZnO, SnO_2, and TiO_2 films used in dye-sensitized solar cells, *ACS Nano*, 2011, **5**, 5158-5166, doi: 10.1021/nn201243y.
[69] A. Wypych, I. Bobowska, M. Tracz, A. Opasinska, S. Kadlubowski, A. Krzywania-Kaliszewska, J. Grobelny, P. Wojciechowski, Dielectric properties and characterisation of titanium dioxide obtained by different chemistry methods, *Journal of Nanomaterials*, 2014, **2014**, 124814, doi: 10.1155/2014/124814.
[70] M. H. Futscher, M. K. Gangishetty, D. N. Congreve, B. Ehrler, Quantifying mobile ions and electronic defects in perovskite-based devices with temperature-dependent capacitance measurements: Frequency vs time domain, *The Journal of Chemical Physics*, 2020, **152**, 044202, doi: 10.1063/1.5132754.
[71] J.-S. Park, J. Calbo, Y.-K. Jung, L. D. Whalley, A. Walsh, Accumulation of deep traps at grain boundaries in halide perovskites, *ACS Energy Letters*, 2019, **4**, 1321-1327, doi: 10.1021/acsenergylett.9b00840.
[72] L. Bertoluzzi, C. C. Boyd, N. Rolston, J. Xu, R. Prasanna, B. C. O′ Regan, M. D. McGehee, Mobile ion concentration measurement and open-access band diagram simulation platform for halide perovskite solar cells, *Joule*, 2020, **4**, 109-127, doi: 10.1016/j.joule.2019.10.003.
[73] G. Richardson, S. E. J. O′ Kane, R. G. Niemann, T. A. Peltola, J. M. Foster, P. J. Cameron, A. B. Walker, can slow-moving ions explain hysteresis in the current–voltage curves of perovskite solar cells, *Energy & Environmental Science*, 2016, **9**, 1476-1485, doi: 10.1039/c5ee02740c.
[74] C. L. Davies, M. R. Filip, J. B. Patel, T. W. Crothers, C. Verdi, A. D. Wright, R. L. Milot, F. Giustino, M. B. Johnston, L. M. Herz, Bimolecular recombination in methylammonium lead triiodide perovskite is an inverse absorption process, *Nature Communications*, 2018, **9**, 293, doi: 10.1038/s41467-017-02670-2.
[75] W. van Roosbroeck, W. Shockley, Photon-radiative recombination of electrons and holes in germanium, *Physical Review*, 1954, **94**, 1558-1560, doi: 10.1103/physrev.94.1558.
[76] F. Xu, J. Zhu, R. Cao, S. Ge, W. Wang, H. Xu, R. Xu, Y. Wu, M. Gao, Z. Ma, F. Hong, Z. Jiang, Elucidating the evolution of the current-voltage characteristics of planar organometal halide perovskite solar cells to an S-shape at low temperature, *Solar Energy Materials and Solar Cells*, 2016, **157**, 981-988, doi: 10.1016/j.solmat.2016.08.011.
[77] W. Peng, C. Aranda, O. M. Bakr, G. Garcia-Belmonte, J. Bisquert, A. Guerrero, Quantification of ionic diffusion in lead halide perovskite single crystals, *ACS Energy Letters*, 2018, **3**, 1477-1481, doi: 10.1021/acsenergylett.8b00641.
[78] K. Domanski, B. Roose, T. Matsui, M. Saliba, S.-H. Turren-Cruz, J.-P. Correa-Baena, C. R. Carmona, G. Richardson, J. M. Foster, F. De Angelis, J. M. Ball, A. Petrozza, N. Mine, M. K. Nazeeruddin, W. Tress, M. Grätzel, U. Steiner, A. Hagfeldt, A. Abate, Migration of cations induces reversible performance losses over day/night cycling in perovskite solar cells, *Energy & Environmental Science*, 2017, **10**, 604-613, doi: 10.1039/c6ee03352k.